Performance of Range and Velocity Estimation in a Multistatic Radar Network with Receiver Swarms

Dilan Dhulashia[1] , Murat Temiz[1], Matthew A Ritchie[1]*

[1]*Department of Electronic and Electrical Engineering, University College London, London, U.K.*
**E-mail: dilan.dhulashia.15@ucl.ac.uk*

Keywords: MULTISTATIC RADAR, CRAMÉR-RAO LOWER BOUNDS, ESTIMATION ERROR, DISTRIBUTED RECEIVERS

Abstract

This research provides an analysis of the theoretical performance of a multistatic radar system comprised of a single active LFM transmitter and many distributed receivers within a swarm. The Cramér-Rao Lower Bounds on the range and velocity estimation errors of a subset of receivers, including the best performers within the swarm, are used as a performance metric and a Monte-Carlo approach is used to simulate the vignettes containing random distributions of node locations. The performance improvement based on the receiver swarm containment volume and number of receivers within the swarm are presented.

1 Introduction

The topic of multistatic radar systems has been the focus of significant research within the radar community for both defence and civilian applications in recent years. Some of the advantages which make such systems highly appealing include their ability to provide: many perspectives, large area coverage, covertness, and frequency and spatial diversity. Within the context of military applications, there is a growing interest in the ability to create radar systems comprised of low-cost and highly manoeuvrable nodes. Such a radar would allow for rapid operational adaptation to varying role requirements and situational changes while enabling each receiver node to be expendable. The Cramér-Rao Lower Bounds (CRLBs) are a well established metric to analyse the theoretical best case performance limits of radar systems for a variety of deterministic parameters.

Previous work has shown how the monostatic CRLBs can be established using the monostatic radar ambiguity function [1] and how this can be extended to bistatic radar configurations through the consideration of node geometry [2]. Prior research has also demonstrated how node pair selection can be effectively achieved in a multistatic system based on the CRLBs [3].

A radar model was established and tested to find the CRLB on range and velocity estimation errors for multistatic hybrid radar network configurations comprised of relatively few nodes in [4]. A similar model has been used to investigate jamming and intentional interference effects on the bounds for similar parameters achievable by such networks in [5].

Investigation into how network node geometry affects the maximum likelihood estimates of range and velocity were investigated for a multistatic configuration consisting of a static staring transmitter (Tx) and three separated receiver (Rx) nodes in [6] and a method for minimising the CRLB was provided. In [7], a single Tx, multiple Rx, multistatic radar was simulated and a method to select weightings to facilitate fusion of data from the multiple Rx nodes based on a multistatic ambiguity function in order to meet a pre-selected performance threshold was presented. It was shown that the choice of fusion strategy is dependent on the radar performance parameter of interest. In another study [8], a method for receiver placement within a multistatic radar system for the purpose of UAV localisation based on the minimisation of parameter estimation errors was shown. The work provides a method to determine the number of receivers needed in the network to meet a performance threshold. The situation considered in this work was limited to 2D space and a condition was made such that placed receivers were all at a fixed distance from a centrally located single target.

The research in this paper acts as novel work by being a first contribution to radar literature in the area of multistatic radar networks comprised of many low gain receivers used in swarm configurations or how such geometries could impact the performance of a multistatic distributed radar system. The abstracted treatment of node group geometries is a further novel feature of the research.

The following sections of this paper are organised as follows: Section 2 presents the main theory behind the calculation of the CRLBs on range and velocity estimation errors; Section 3 describes the methodology used for the simulations; Section 4 presents the results obtained in the simulations carried out. Finally, Section 5 concludes the work.

2 Theory

2.1 Bistatic radar measurements

A multistatic radar network can be thought of as a collection of bistatic radars that operate in a collaborative manner. The simulation of a multistatic system can thus be realised by considering each transmitter-receiver (Tx-Rx) pair within the system as an individual bistatic radar. Calculation of the CRLB on bistatic range and velocity, as used in this work, requires a bistatic ambiguity function which accounts for geometry,

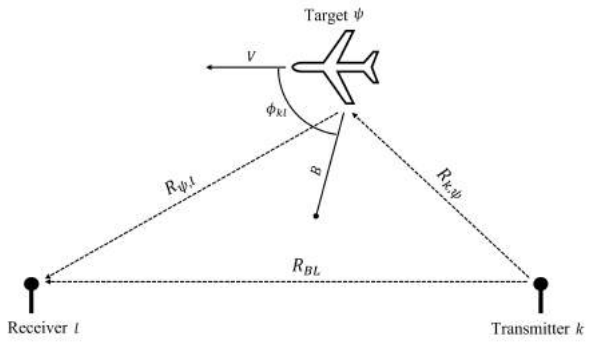

Fig. 1: Bistatic radar geometry in a North coordinate system

which has been derived in [9]. A North coordinate system bistatic configuration is shown in Fig 1, where the distance between Tx k and target ψ is $R_{k,\psi}$, the distance between target ψ and Rx l is $R_{\psi,l}$, and the baseline distance is denoted R_{BL}. (This parameter should not be confused with the symbol $R_{l,k}$, which is later used to denote the bistatic range between Tx k, target ψ, and Rx l). The bistatic radial velocity of the target is given by $V_{radial} = Vcos\phi_{kl}$, where V denotes the velocity of the target.

The bistatic operation of each Tx-Rx pair within a radar network requires two channels. The reference channel obtains a copy of the transmitted radar waveform directly from the emission from the transmitter, while the surveillance channel obtains the transmitted waveform after reflection from a target in the vicinity. Signal models for the received waveforms at the reference and surveillance channels can therefore be derived by considering the geometry presented in Fig 1 and are given in [5]. In the case where only receiver noise is considered with no additional interference (e.g. electronic countermeasures), the instantaneous SNR at Rx l due to a transmission from Tx k which has been reflected from target ψ can be expressed as

$$\rho_{l|k,\psi} = \frac{P_k G_k G_l \sigma_{l|\psi} \left[\gamma_{k\psi} + \gamma_{\psi l}\right]}{2k_B T_{0_l} B_l N_{F_l} + \mu_{DPI} P_k(t) G_k(t) G_l(t) \gamma_{kl}}, \quad (1)$$

where P_k is the transmit power of Tx k, G_k and G_l are the gains of Tx k and Rx l, respectively, $\sigma_{l|\psi}(t)$ is the RCS of the target ψ observed from Rx l, γ_{ab} is the path loss between entity a and b, μ_{DPI} is the residual direct-path interference (DPI) ratio which acts as a coefficient measuring the effectiveness of the DPI cancellation scheme used by the passive radar, k_B is the Boltzmann constant, and T_{0_l}, B_l, and N_{F_l} are the temperature, bandwidth, and noise figure of receiver l, respectively. In the simulations carried out in this research, a value for μ_{DPI} is chosen such that 50 dB of suppression is assumed for the direct path return. The target RCS and the path losses are chosen to be time independent and target RCS is also simplified to be aspect angle independent.

2.2 Cramér-Rao Lower Bounds

The CRLB describes the minimum variance which can be expected of an unbiased estimator for a deterministic parameter. That is, an estimator possessing an expected value equal to the true parameter value. The CRLB is therefore considered a highly effective measure for the analysis of the best case performance of a radar system in obtaining the range and velocity measurements of a target. The CRLB is defined as the inverse of the Fisher Information Matrix (FIM) and has previously been used for the analysis of radar performance for range and velocity estimation errors in [5]. It should be noted that the conventional syntax used to denote element x, y of a matrix given by $\mathbf{A}$ is employed in the following equations, i.e. $[\mathbf{A}]_{x,y}$.

Following the provided definition, the bistatic CRLB on the range and velocity estimation errors can be found using the bistatic FIM. The FIM for the Tx-Rx pair between Tx k and Rx l is then given by

$$\mathbf{J}(R_{l,k}, V_{l,k}) = -2\rho_{l,k} \begin{bmatrix} \frac{\partial^2 \Theta\left(R_{l,k}, V_{l,k}\right)}{\partial R_{l,k}^2} & \frac{\partial^2 \Theta\left(R_{l,k}, V_{l,k}\right)}{\partial R_{l,k} \partial V_{l,k}} \\ \frac{\partial^2 \Theta\left(R_{l,k}, V_{l,k}\right)}{\partial V_{l,k} \partial R_{l,k}} & \frac{\partial^2 \Theta\left(R_{l,k}, V_{l,k}\right)}{\partial V_{l,k}^2} \end{bmatrix}, \quad (2)$$

where $\rho_{l,k}$ is the SNR as derived in Equation (1), $R_{l,k}$ and $V_{l,k}$ are the bistatic range and velocity observed between the Tx-Rx pair, and each element is some second partial derivative of the bistatic ambiguity function denoted by $\Theta\left(R_{l,k}, V_{l,k}\right)$. Each of the elements within the bistatic FIM can be shown to be comprised of a sum of products between partial derivatives relating to the bistatic geometry with the waveform only FIM. Explicitly, the elements of the bistatic FIM have been shown in [2] along with the bistatic geometry based derivatives with respect to bistatic range and velocity. The waveform only FIM for a LFM waveform is given by [1]

$$\mathbf{J}_0 = \begin{bmatrix} \frac{\partial^2 \Theta(\tau,\omega)}{\partial \tau^2} & \frac{\partial^2 \Theta(\tau,\omega)}{\partial \tau \partial \omega} \\ \frac{\partial^2 \Theta(\tau,\omega)}{\partial \omega \partial \tau} & \frac{\partial^2 \Theta(\tau,\omega)}{\partial \omega^2} \end{bmatrix} = \begin{bmatrix} \frac{-\pi^2 f_B^2}{3} & \frac{\pi^2 f_B T_C}{3} \\ \frac{\pi^2 f_B T_C}{3} & \frac{\pi^2 T_R (1-N^2) - \pi^2 T_C^2}{3} \end{bmatrix}, \quad (3)$$

where T_C is the chirp length, T_R is the chirp repetition period, N the number of chirps transmitted, and f_B is the bandwidth of the chirp.

The CRLB on bistatic range and velocity, which provides the lower bound on the variance (i.e. the estimation error), between Tx k and Rx l are then given by

$$CRLB(R_{l,k}) = \frac{[\mathbf{J}(R_{l,k}, V_{l,k})]_{2,2}}{\det\left[\mathbf{J}(R_{l,k}, V_{l,k})\right]}, \quad (4)$$

$$CRLB(V_{l,k}) = \frac{[\mathbf{J}(R_{l,k}, V_{l,k})]_{1,1}}{\det\left[\mathbf{J}(R_{l,k}, V_{l,k})\right]}, \quad (5)$$

where $\mathbf{J}(R_{l,k}, V_{l,k})$ is the bistatic FIM between Tx k and Rx l, as defined in 2.

3 Methodology

The research presented in this paper is broadly split into two investigations. The procedures employed in these are described in subsections 3.1 and 3.2. In the synthesis of the data from each of these investigations, two averaging methods are used. These are described in subsection 3.3.

3.1 Investigation I

The first investigation concentrates on the effect of the number of Rx nodes within a multistatic radar network on the parameter estimation error. A scenario vignette including a single airborne target and a single active LFM radar transmitter is used and a simulated situation involving the target traversing a defined flight path over the course of the simulation runtime is constructed.

The number of Rx nodes within the network is used as an investigation parameter such that a particular number of Monte-Carlo simulations are carried out to determine the network performance for each of the Rx number values to be tested. For a given amount of Rx nodes, the positions of each Rx node within the swarm are randomly chosen for each Monte-Carlo repetition. The target flight path and the Tx node position are kept constant for all Monte-Carlo repetitions for all amounts of Rx nodes investigated.

A map of an example of relative node and target positions throughout a given simulation is shown in Fig 2. In the example depicted, a simulation containing 25 Rx nodes is used.

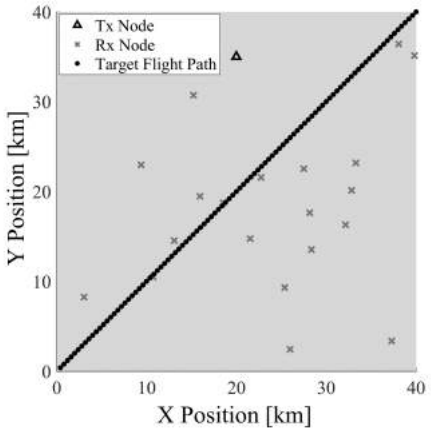

Fig. 2: Top down view of scenario map, showing flight path, Tx position, and example of 25 Rx nodes randomly distributed throughout map

Table 1 shows the different test parameter values used within the investigation. It should be noted that where ranges are given, only some particular discrete values within these ranges are chosen.

Table 1 Investigation I test parameters

Parameter	Value
Tx Position	(20000, 35000, 5) m
Rx Positions	Random
No. Rx in Swarm (NRxS)	8-50
Monte-Carlo Repetitions per NRxS	100
Simulation Runtime	100 s
Target Position at Time = t	(400t, 400t, 400) m
Map Bounding Ranges	(40000, 40000, 500) m

3.2 Investigation II

The second investigation concentrates on spatially constrained swarms within an imaginary cylindrical bounding volume. That is, all Rx nodes within the swarm must be randomly distributed within the volume. The effects of both bounding volume size and number of Rx nodes within the swarm on parameter estimation error are simultaneously determined.

The imaginary cylindrical bounding volume used is defined by the: cylinder diameter, C_d, cylinder height, C_h and cylinder centre point, (C_x, C_y), which lies at the mid-height of the cylinder and inline with the central points of the end circles. The centre point of the cylinder is randomly chosen for each Monte-Carlo repetition carried out in the investigation, and it is ensured that the cylindrical volume is always entirely contained within the scenario map limits. Investigation II can then be broadly split into two further sub-categories based on the positioning of the imaginary cylindrical bounding volume. The first (Investigation II-A) is concerned with cases where the bounding volume has no intersection with the target throughout the runtime of the simulation (i.e. no intersection with the target flight path). The second (Investigation II-B) is concerned with cases where the bounding volume has a guaranteed intersection with the target path for some period within the simulation runtime. Examples of the two subcategory cases are shown in Fig 3.

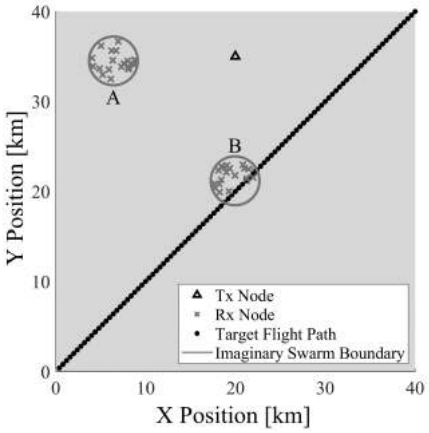

Fig. 3: Top down view of scenario map for Investigation II, showing two 20 Rx node distributions within a 5 km diameter bounding cylindrical volumes: A) non-intersecting with target path and B) intersecting with target path.

It should be noted that the examples shown in Fig 3 were specifically chosen to show separation between target path and swarm bounding volume such that in the top down view, the separation can be seen in the XY-plane. It is, however, possible for the separation to occur along the Z-axis (i.e. in elevation). The bounding volume height is kept constant in all trials within Investigation II.

The test parameters used for Investigation II are shown in Table 2. It can be seen that the same number of Monte-Carlo trials are carried out for each boundary volume and Rx number in swarm combination and for both Investigation II-A and II-B. The tested boundary diameters and number of Rx nodes in swarm are also included in Table 2.

Table 2 Investigation II test parameters

Parameter	Value in II-A	Value in II-B
No. Rx in Swarm (NRxS)	8-50	8-50
Boundary Diameter	0.25-25 km	0.25-25 km
Boundary Height	100 m	100 m
Boundary Centre Point	Random	Random
Boundary-Target Intersect	False	True

The output data obtained from each trial carried out in Investigation I and II (where a single trial is defined as the simulation of a scenario runtime for a single situation configuration) consists of two matrices with each row corresponding to a particular Rx node and each column corresponding to a measurement instance within the runtime. The values contained within the elements of the matrix are then the square-root CRLB (RCRLB) on range estimation error (first matrix) and on velocity estimation error (second matrix) for each Rx node at each time instance. The Tx and Rx operating characteristics and waveform parameters used are shown in Table 3.

Table 3 Tx, Rx, and waveform parameter values used

Parameter	Value
Tx Power	5000 W
Tx Gain	30 dB
Rx Gain	2.15 dB
Chirp Carrier Frequency	10 GHz
Chirp Bandwidth (f_B)	50 MHz
Chirp Length (T_C)	200 μs
Chirp Repetition Interval (T_R)	400 μs
Chirps in Processing Interval (N)	64

3.3 Averaging Methods

Two averaging methods (Method I and Method II) are used in this research and are described by Algorithm I and Algorithm II, respectively. Method I provides the theoretical best case results based on the time interval resolution used in the simulations. Method II provides an insight into results which are likely more representative of a network which employs averaging over multiple nodes and a longer interval between updating node selection.

The input and output variables used within the two averaging algorithms defined in Algorithm I and II include: the number of Monte-Carlo repetitions for a given choice of test parameters M, the set of input Rx-RCRLB matrices $\mathbf{X_1}, ..., \mathbf{X_M}$, the discrete number of processing segments into which the runtime is divided N_{ps}, the discrete number of measurements within a segment N_{seg}, and a selection threshold S_{thresh}, which determines the number of receivers to be used for analysis (i.e. the size of the selected subset of receivers). Other terms which appear in the algorithms are self contained and have no relation to similarly symbolised terms appearing elsewhere in this paper. A conventional style is used such that matrices are denoted using capitalised, boldface, vectors with lower-case, boldface, and scalar quantities with non-boldface symbols.

Algorithm I: Method I algorithm

Input: $\mathbf{X}_1, ..., \mathbf{X}_M, M$

Output: $\bar{x}, c_v$

Mean and coefficient of variation over Monte-Carlo trials for minimum RCRLB at each time instance

for $i \leftarrow 1$ **to** M **do**
  $Y \leftarrow 0$
  $\mathbf{R} \leftarrow \mathbf{X}_i$
  for $j \leftarrow 1$ **to** $len(\mathbf{R}, cols)$ **do**
    $Y \leftarrow Y + min(\mathbf{R}_{:,j})$
  end
  $\mathbf{a}_i \leftarrow \frac{Y}{len(\mathbf{R}, cols)}$
end

$\bar{x} \leftarrow \frac{\sum_{k\leftarrow 1}^{M} \mathbf{a}_k}{M}$

$c_v \leftarrow \frac{\sqrt{\frac{\sum_{k\leftarrow 1}^{M} (\mathbf{a}_k - \bar{x})^2}{M-1}}}{\bar{x}}$

Algorithm II: Method II algorithm

Input: $\mathbf{X}_1, ..., \mathbf{X}_M, M, N_{seg}, N_{ps}, S_{thresh}$

Output: $\bar{x}, c_v$

Mean and coefficient of variation over Monte-Carlo trials for lowest S_{thresh} RCRLB at each interval of N_{ps}

for $i \leftarrow 1$ **to** M **do**
  $\mathbf{R} \leftarrow \mathbf{X}_i$
  for $n \leftarrow 1$ **to** N_{ps} **do**
    $\mathbf{U} \leftarrow \mathbf{R}_{:,(n-1)N_{seg}+1:nN_{seg}})$
    for $j \leftarrow 1$ **to** $len(\mathbf{U}, rows)$ **do**
      $\mathbf{l}_j \leftarrow \frac{\sum_{k\leftarrow 1}^{len(\mathbf{U},cols)} \mathbf{U}_{j,k}}{N_{seg}}$
    end
    $\mathbf{o} \leftarrow sort(\mathbf{l}, ascending)$
    $\mathbf{p}_n \leftarrow \frac{\sum_{k\leftarrow 1}^{S_{thresh}} \mathbf{o}_k}{S_{thresh}}$
  end
  $\mathbf{q}_i \leftarrow \frac{\sum_{k\leftarrow 1}^{N_{ps}} \mathbf{p}_k}{N_{ps}}$
end

$\bar{x} \leftarrow \frac{\sum_{k\leftarrow 1}^{M} \mathbf{q}_k}{M}$

$c_v \leftarrow \frac{\sqrt{\frac{\sum_{k\leftarrow 1}^{M} (\mathbf{q}_k - \bar{x})^2}{M-1}}}{\bar{x}}$

The outputs from Method I and II are the mean value $\bar{x}$ and a coefficient of variation c_v for both the range and the velocity for an entire set of Monte-Carlo trials for each selection of independent parameters used. Here, an independent parameter set is considered to be either the number of Rx nodes within a swarm (for Investigation I) or the number of Rx nodes within a swarm and the swarm diameter (for Investigation II). These mean and coefficient of variation values are presented in the results of this paper.

4 Simulations and Numerical Results

4.1 Investigation I

The results obtained from the simulations described in subsection 3.1 are presented here. The average of the RCRLB on range and velocity as found using both averaging methods are shown in Fig 4, along with the coefficient of variation.

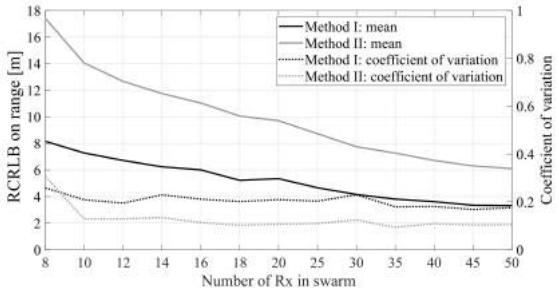

(a)

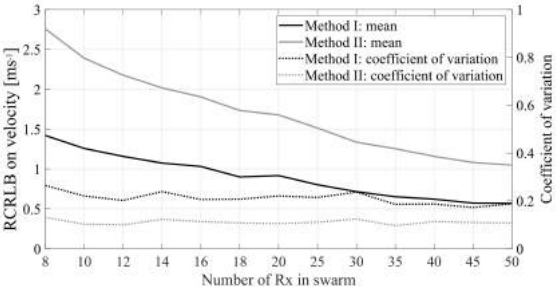

(b)

Fig. 4: Mean and coefficient of variation, taken across 100 Monte-Carlo trial outcomes for each Rx quantity, of RCRLB on: (a) range and (b) velocity, found using both averaging methods

An improvement can be seen in the RCRLB on both range and velocity from Figs 4a and 4b, respectively, when using both averaging methods. This improvement shows diminishing returns as the number of Rx nodes increases, with the greatest improvement per additional node being realised when the number of existing nodes is low. In both the range and velocity cases, it can be seen that the coefficient of variation is relatively constant across the number of Rx nodes used, meaning the amount of variation across the Monte-Carlo trial sets simulated for the different test parameters was consistent. The estimation error for both parameters is lower when using the Method I averaging procedure compared to when Method II is used (as expected), but the amount of estimation error improvement from using Method I over Method II decreases as the number of Rx nodes used increases. The coefficient of variation tends to be lower for the results obtained via Method I which is understandable given the greater number of nodes averaged over at each time interval in this case.

4.2 Investigation II

The results obtained from both Investigations II-A and 2B are presented here. The results from these two parts have been combined within Fig 5 for both range and velocity, as well as for both averaging methods, in order to facilitate comparison of performance for the two geometry classes addressed by Investigations II-A and II-B.

Comparison of Figs 5a and 5b with Figs 5c and 5d show that a significant difference in performance is observed depending on whether or not the Rx swarm intersects with the flight path over some period of time during the simulations. In cases where intersection occurs, substantially better performance is achieved compared to corresponding cases without intersection. When an intersection does occur, the performance is relatively uniform regardless of the number of Rx nodes within the swarm or the swarm boundary volume diameter. In such cases, only minor improvements in estimation error of range for larger boundary sizes is observed. Velocity estimation errors have a greater dependence on swarm volume diameter in the results from the intersection tests in Investigation II-B. However, when no intersection occurs, there is a great dependence of performance on the swarm boundary diameter, with larger diameters producing much better (i.e. lower) estimation errors for both range and velocity. There is also a dependence on the number of Rx nodes within the swarm; however, this appears less significant than the dependence on swarm boundary diameter from the results obtained. All the surfaces obtained show an acuter steepness along the dimension corresponding to the number of Rx in the swarm compared to the steepness in the dimension of the swarm boundary volume diameter.

It is further observed that greater variance is observed in the estimation error achieved for different numbers of Rx nodes within the swarm when the boundary volume is small compared to when the boundary volume is large. This is particularly noticeable in the surfaces shown in Figs 5a and 5b. It can also be seen from comparing Fig 5a with 5b, 5c with 5d, 5e with 5f, and 5g with 5h, that the same minor advantage is seen from using Method I averaging over Method II in all cases, with the significance of this being reduced as the number of Rx nodes increases.

The results provide quantitative evidence that the best performance in terms of estimation error reduction can be achieved by using a larger number of Rx nodes within a swarm and distributing them over a larger area. This is particularly important if the Rx swarm is located at an offset distance from the target trajectory with no chance of intersection. The swarm boundary

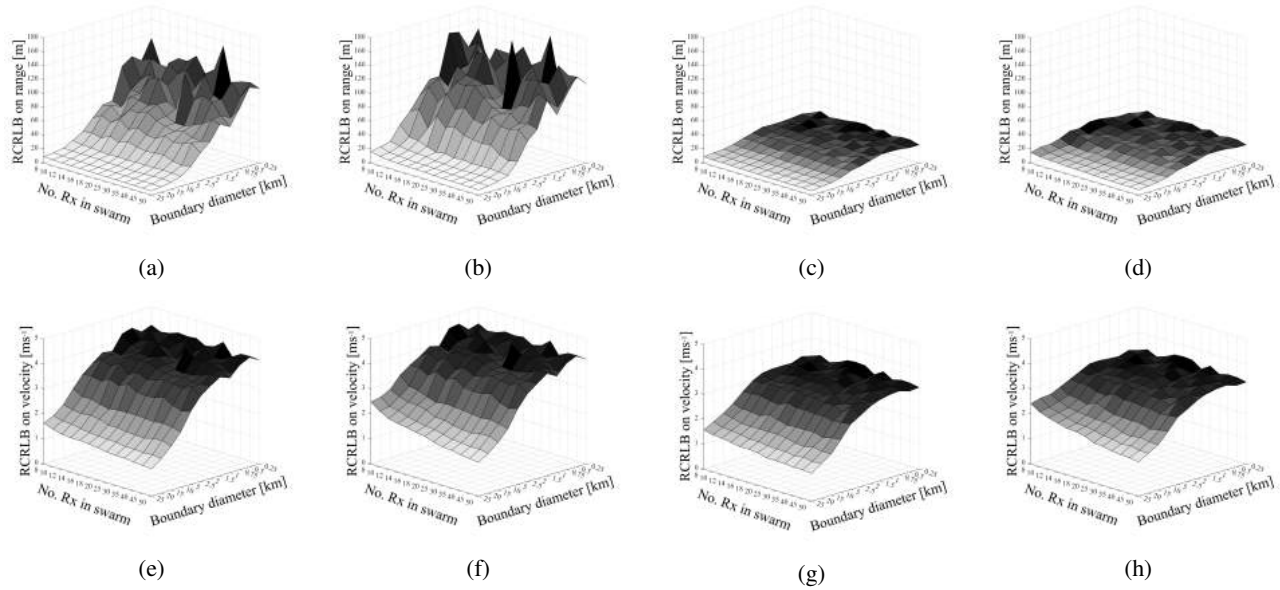

Fig. 5: RCRLB on range: (a) Investigation II-A using Method I averaging (b) Investigation II-A using Method II averaging (c) Investigation II-B using Method I averaging (d) Investigation II-B using Method II averaging, and on velocity: (e) Investigation II-A using Method I averaging (f) Investigation II-A using Method II averaging (g) Investigation II-B using Method I averaging (h) Investigation II-B using Method II averaging, averaged over Monte-Carlo trials for each swarm boundary radius and receiver population quantity

area is of greater importance over the number of nodes being used when Rx nodes are randomly positioned, according to the surfaces obtained in Investigations II-A and II-B.

5 Conclusion

In this research the RCRLB on the bistatic range and velocity are used to analyse the performance dependence of a multistatic Rx swarm radar network on the number of Rx nodes in the swarm and the swarm occupation volume. The results indicate that the performance level is largely based on the diameter of the swarm boundary and that significantly better performance can be achieved when using lower quantities of Rx nodes or smaller swarm boundaries if the swarm is situated such that the target passes through the swarm area.

6 Acknowledgements

This work was supported in part by the Engineering and Physical Sciences Research Council (EPSRC) under grant number: EP/R513143/1, Thales UK, University Defence Research Collaboration (UDRC) and the Defence Science and Technology Laboratory (Dstl).

7 References

[1] Dogandzic, A., Nehorai, A.: 'Cramér-rao bounds for estimating range, velocity, and direction with an active array', IEEE Transactions on Signal Processing, June 2001, vol. 49, no. 6, pp. 1122–1137.

[2] Greco, M. S., Stinco, P., Gini, F., et al.: 'Cramér-Rao bounds and selection of bistatic channels for multistatic radar systems', IEEE Transactions on Aerospace and Electronic Systems, October 2011, vol. 47, no. 4, pp. 2934–2948.

[3] Greco, M. S., Stinco, P., Gini, F., et al.: 'Cramér-Rao bounds and Tx-Rx selection in a multistatic radar scenario', 2010 IEEE Radar Conference, May 2010, pp. 1371–1376.

[4] Temiz, M., Ritchie, M. A., and Griffiths, H. D.: 'Waveform Selection For Multi-Band Multistatic Radar Networks', TechRxiv. Preprint. https://doi.org/10.36227/techrxiv.19329497.v1

[5] Dhulashia, D., Temiz, M. and Ritchie, M. A.: 'Jamming Effects on Hybrid Multistatic Radar Network Range and Velocity Estimation Errors', IEEE Access, 2022, vol. 10, pp. 27736-27749.

[6] Griffin, B., Balleri, A., Baker, C., et al.: 'Optimal receiver placement in staring cooperative radar networks for detection of drones', 2020 IEEE Radar Conference (RadarConf20). IEEE, 2020, pp. 1–6.

[7] Bradaric, I., Capraro, G. T., Weiner, et al.: 'Multistatic radar systems signal processing', Proc. IEEE International Conference on Radar, New York, NY, USA, April 2006, pp. 106–113.

[8] Leba, P., Baudais, J., Méric, S., et al.: 'Receivers placement for UAV localization in a surveillance area'. Proc. 18th European Radar Conf, London, U.K., April 2022, pp. 1–4.

[9] T. Tsao, M. Slamani, P. Varshney, et al.,: 'Ambiguity function for a bistatic radar', IEEE Transactions on Aerospace and Electronic Systems, July 1997, vol. 33, no. 3, pp. 1041–1051.